

XY-like Incommensurate Magnetic Order in Ce₂SnS₅

Maximilien Debbas,¹ Takehito Suzuki,² and Joseph G. Checkelsky³

¹*Department of Nuclear Science and Engineering,
Massachusetts Institute of Technology, Cambridge, MA 02139, USA*

²*Department of Physics, Toho University, Funabashi, Japan*

³*Department of Physics, Massachusetts Institute of Technology, Cambridge, MA 02139, USA*
(Dated: March 12, 2025)

We report the synthesis of single crystals of Ce₂SnS₅ through a two-stage chemical vapor transport method. The Ce₂SnS₅ system is a member of the orthorhombic *Pbam* (No. 55) space group and realizes a distorted trigonal tricapped prism (TTP) crystal field around each cerium site. We characterized the sample through orientation-dependent magnetization and heat capacity measurements to probe the magnetic anisotropy in the system characteristic of XY-like anisotropic Heisenberg model behavior. Ce₂SnS₅ furthermore enters a zero-field ordered phase under $T_N = 2.4$ K; powder neutron diffraction measurements reveal incommensurate magnetic order near T_N . The system locks into a commensurate structure with a $(q_x, q_y, q_z) = (1/3, 0, 0)$ propagation vector below approximately 1.2 K.

I. INTRODUCTION

Antiferromagnetic systems such as the MPS₃ family [1–3] and the BaM₂(XO₄)₂ [4] family provide physical examples of three dimensional systems realizing anisotropic Heisenberg model physics. The general Hamiltonian given by:

$$\mathbf{H} = -2 \sum_{i < j} (J_{\perp} (\mathbf{S}_i^x \mathbf{S}_j^x + \mathbf{S}_i^y \mathbf{S}_j^y) + J_{\parallel} \mathbf{S}_i^z \mathbf{S}_j^z) \quad (1)$$

where the summation is generally taken over the neighboring sites i, j in the lattice, describes the Ising model when $J_{\perp} = 0$, the XY model when $J_{\parallel} = 0$, and the isotropic Heisenberg model when $J_{\perp} = J_{\parallel}$ [5]. In real bulk systems, however, the exchange couplings J_{\perp} and J_{\parallel} are typically relatively isotropic; anisotropic Ising or XY model physics generally arise from spin-orbit coupling and crystal field effects [5]. The axial distortion induced by a crystal field modifies the isotropic Heisenberg Hamiltonian to the following form:

$$\mathbf{H} = -2J \sum_{i < j} \vec{\mathbf{S}}_i \cdot \vec{\mathbf{S}}_j - D \sum_i (\mathbf{S}_i^z)^2 \quad (2)$$

where $D \rightarrow +\infty$ describes an Ising system, and $D \rightarrow -\infty$ describes an XY system [5]. Experimentally, the anisotropy of the g-tensor differentiates an Ising system ($g_z \gg g_x, g_y$) from an XY system ($g_x \approx g_y \gg g_z$) [5]. We report here that the Ce₂SnS₅ system may realize XY-like magnetism induced by a highly anisotropic crystal field surrounding the cerium site.

The magnetic behavior of Ce₂SnS₅ is probed via measurements of the magnetization. This quantity (along with the derived magnetic susceptibility) are obtained from the free energy of the system as:

$$M_T = - \left(\frac{\partial F}{\partial H} \right)_T \quad (3)$$

$$\chi_T = \left(\frac{\partial M}{\partial H} \right)_T = - \left(\frac{\partial^2 F}{\partial H^2} \right)_T \quad (4)$$

where M_T is the isothermal magnetization, χ_T is the isothermal magnetic susceptibility, F is the free energy, and H is the applied field strength [5]. For small applied fields, the magnetic susceptibility may be approximated as $\chi \approx M/H$.

Ce₂SnS₅ is a member of the centrosymmetric *Pbam* space group and realizes the La₂SnS₅ crystal structure. There exists a previous structural report for La₂SnS₅ on ~ 100 μm large single crystals obtained in mapping the the Ln₂S₃-SnS₂ (Ln = lanthanide) phase diagram [6]. Another literature report on the Ln₂X₃-SnX₂ (Ln = lanthanide, X = S or Se) phase diagram also contains some additional structural data for Ce₂SnS₅ [7].

We report herein a vapor transport method for growing large, high-quality single crystals of Ce₂SnS₅. Through orientation-dependent magnetization and heat capacity measurements, we find evidence for a planar ordering of magnetic moments primarily in the *ab*-plane of the crystal. Through powder neutron diffraction, we additionally find evidence for incommensurate order in the zero-field, low-temperature phase. Due to the strong magnetic anisotropy discovered in this system, Ce₂SnS₅ provides a new opportunity to study XY-like Heisenberg physics in a physical system.

II. GROWTH METHOD

Single crystals of Ce₂SnS₅ were synthesized using a two-part growth methodology. The first phase involved reacting the constituent elements at high temperature followed by subsequent regrinding steps to obtain extremely pure Ce₂SnS₅ powder. The second phase utilized chemical vapor transport (CVT) of this powder

with a chloride transport agent. The materials used were 99.9% purity (metals basis excluding Ta) cerium rod (Thermo Scientific), 99.995% purity, -100 mesh tin powder (Thermo Scientific), 99.9995% purity sulfur pieces (Thermo Scientific), and $\geq 99.99\%$ purity tin (II) chloride (Sigma Aldrich).

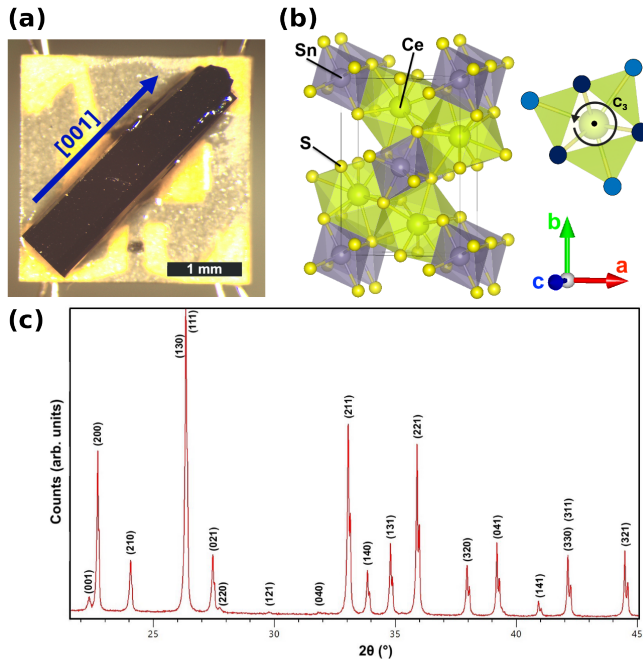


FIG. 1. (a) Ce_2SnS_5 single crystal prepared for a heat capacity measurement with the [001] direction indicated by the blue arrow. (b) Ce_2SnS_5 crystal structure showing the cerium in green, the sulfur in yellow, and the tin in purple. The coordination polyhedron around each cerium site is shown on the right with the C_3 symmetry axis of the undistorted polyhedron labeled and the sulfur atoms forming the polyhedron drawn in blue (the dark blue atoms lie in the plane of the page whereas the light blue atoms lie in a plane behind that of the page). Crystal structure drawn using VESTA [8]. (c) Powder XRD pattern of material obtained at the end of the first synthesis phase. The (hkl) indices of the Ce_2SnS_5 peaks are labeled.

For the first phase, a chunk of cerium rod was clipped off and placed into an alumina crucible along with a stoichiometric amount of tin powder and sulfur. This was done under argon in a glovebox, and the alumina crucible containing the starting materials was sealed under high vacuum in a quartz tube. The tube was then heated to 900°C over 36 hours, held at that temperature for 48 hours, cooled to 400°C over a week, and then finally cooled to room temperature over 12 hours. After this initial step, two regrinding steps were performed during which the material from the previous step was ground using a mortar and pestle and resealed in a quartz tube under vacuum. The resealed tube was then heated to 850°C over eight hours, held at that temperature for five days, and then finally cooled to room temperature over

eight hours. The purity of the material was checked after each step using powder x-ray diffraction (XRD); the XRD spectrum after the final step is shown in Figure 1(c).

For the second phase, a chloride CVT growth was done using Ce_2SnS_5 powder from the previous phase and a small amount of tin (II) chloride ($0.258 \text{ mol}_{\text{SnCl}_2}/\text{mol}_{\text{Ce}_2\text{SnS}_5}$). The materials were sealed inside a 300 mm long, 12 mm diameter quartz tube under high vacuum and placed in a two-zone tube furnace such that end of the tube containing the starting materials was put at the hot zone and the opposite end was put at the cold zone. The tube was heated up over 12 hours, the hot/cold zones held at $850^\circ\text{C}/800^\circ\text{C}$ respectively for 300 hours, and then cooled to room temperature over 12 hours. This was repeated two additional times. At the end of the final stage, several few mm long, prism-shaped crystals of Ce_2SnS_5 had formed at the hot end. Figure 1(a) shows one of the single crystals obtained from this synthesis batch.

III. CRYSTAL STRUCTURE

The Ce_2SnS_5 system is a member of the orthorhombic $Pbam$ (55) space group. The structure (shown in Figure 1(b)) possesses a single mirror symmetry in the ab -plane and two half-cell glide symmetries along the a and b axes. The crystals all realized a prismatic morphology with the [001] direction (c -axis) parallel to the long dimension of the prism. This orientation was determined via Laue x-ray diffraction on several single crystals from the synthesis batch.

Each cerium atom coordinates with nine nearest neighbor sulfur atoms which form a slightly distorted tri-capped trigonal prism (TTP) coordination polyhedron (shown to the right of Fig. 1(b)). Were it undistorted, this coordination polyhedron would realize the point group D_{3h} with the C_3 rotational axis of the polyhedron aligned parallel to the c -axis. The distortion may be considered in two “steps” as $D_{3h} \rightarrow C_{2v} \rightarrow C_s$. The $D_{3h} \rightarrow C_{2v}$ step accounts for the vast majority of the distortion effects as the $C_{2v} \rightarrow C_s$ step is slight. The coordination polyhedron is well-modeled by an ionic crystal field where the sulfur realizes S^{2-} and the cerium realizes Ce^{3+} .

A. Crystal Field Splitting

The coordination polyhedron formed by the nine S^{2-} ions causes crystal field splitting of the localized $4f$ -electron of the Ce^{3+} ion at the center of the polyhedron. Due to strong spin-orbit coupling in rare earth systems, the single $4f$ -electron couples to the orbital angular momentum to yield a sixfold degenerate ground state multiplet $^2F_{5/2}$ and an eightfold degenerate excited state multiplet $^2F_{7/2}$. The Ce^{3+} free-space spin-orbit coupling be-

tween these two multiplets of 3150 K is far larger than both the crystal field splitting and laboratory temperature scales [9]. The excited state multiplet ${}^2F_{7/2}$ may thereby be ignored.

As the ground state multiplet ${}^2F_{5/2}$ is characterized by the half-quantized total angular momentum $J = 5/2$, the crystal field splitting must be analyzed using the crystal double group of the coordination polyhedron due to the odd parity of ${}^2F_{5/2}$ under a 2π rotation [10]. The ${}^2F_{5/2}$ multiplet is then subjected to the double group D'_{3h} in the undistorted crystal field such that the ${}^2F_{5/2}$ multiplet breaks up into the three, doublet irreducible representations $\Gamma_7 \oplus \Gamma_8 \oplus \Gamma_9$.

The first distortion step lowers the symmetry to the double group C'_{2v} such that the ${}^2F_{5/2}$ multiplet breaks up into three copies of the Γ_5 Kramers' doublet (*i.e.*, $3\Gamma_5$). Should the distortion be considered in its entirety, the symmetry would formally be lowered to the double group C'_s such that the ${}^2F_{5/2}$ multiplet breaks up into three copies of the $\Gamma_{3,4}$ Kramers' doublet (*i.e.*, $3\Gamma_{3,4}$). Both distortions preserve the energy level structure as they simply shift the energies of the Kramers' doublets. The level structure of Ce^{3+} may then be modeled as a three level system of doublets even when distortion of the crystal field is considered.

B. Magnetic Anisotropy

As the distortion is slight, the Kramers' pairs will be considered here for the undistorted D'_{3h} double group. The generic crystal electric field (CEF) potential for a TTP ligand field is given by Eq. (5):

$$V_{TTP} = B_0^2 C_0^2 + B_0^4 C_0^4 + B_0^6 C_0^6 + B_6^6 (C_{-6}^6 + C_6^6) \quad (5)$$

$$C_q^k(\theta, \phi) = \sqrt{\frac{4\pi}{2k+1}} Y_k^q(\theta, \phi) \quad (6)$$

where B_q^k are the crystal field parameters, and $C_q^k(\theta, \phi)$ are tensor operators (related to the spherical harmonics $Y_k^q(\theta, \phi)$ via Eq. (6)) [11]. The polar angles θ, ϕ are defined relative to the C_3 rotation axis of the crystal field, *i.e.*, along the c -axis of the crystal. Treating V_{TTP} as a perturbation and diagonalizing it in the $|J = 5/2, m_J\rangle$ basis yields the following degenerate pairs of wavefunctions:

$$\Gamma_7 : |\psi_{\pm 1/2}\rangle = |5/2, \pm 1/2\rangle \quad (7)$$

$$\Gamma_8 : |\psi_{\pm 3/2}\rangle = |5/2, \pm 3/2\rangle \quad (8)$$

$$\Gamma_9 : |\psi_{\pm 5/2}\rangle = |5/2, \pm 5/2\rangle \quad (9)$$

each corresponding to a Kramers' doublet in the TTP energy level structure. Computing the g-tensor associated with each of these degenerate subspaces (see Appendix A) yields:

$$|\psi_{\pm 1/2}\rangle : g_{\parallel} = \frac{6}{7} \quad g_{\perp} = \frac{18}{7} \quad (10)$$

$$|\psi_{\pm 3/2}\rangle : g_{\parallel} = \frac{18}{7} \quad g_{\perp} = 0 \quad (11)$$

$$|\psi_{\pm 5/2}\rangle : g_{\parallel} = \frac{30}{7} \quad g_{\perp} = 0 \quad (12)$$

which highlights the magnetic anisotropy of the system compared to the isotropic Landé g-factor of $g_{J=5/2} = 6/7$. Including the effects of the distortion will mix other components of $|J = 5/2, m_J\rangle$ into the wavefunctions spanning each degenerate subspace and will result in nonzero values of g_{\parallel} and g_{\perp} for each of the Kramers' doublets.

IV. MEASUREMENTS

Herein, we present results derived from magnetization and heat capacity measurements of three Ce_2SnS_5 single crystals (*A*, *B*, and *C*) which were grown in the same synthesis batch. Note that the Ce_2SnS_5 system was found to be an electrical insulator. We also present results from a zero-field powder neutron diffraction measurement performed at Oak Ridge National Laboratory.

A. Magnetization

Magnetization M was measured using SQUID magnetometry in a Quantum Design MPMS3 system. Single crystals were affixed to a quartz rod using GE varnish and DC magnetization measurements were performed using Vibrating Sample Magnetometer (VSM) mode.

Figure 2(a) shows the magnetic susceptibility of Ce_2SnS_5 with the field aligned perpendicular to the c -axis (black) and parallel to the c -axis (blue). The inset shows the low temperature magnetic susceptibility; a peak is visible at $T_N = 2.4\text{K}$ when the field is aligned perpendicular to the c -axis, and a corresponding kink appears when the field is aligned parallel to the c -axis. These features indicate the onset of a magnetic phase transition.

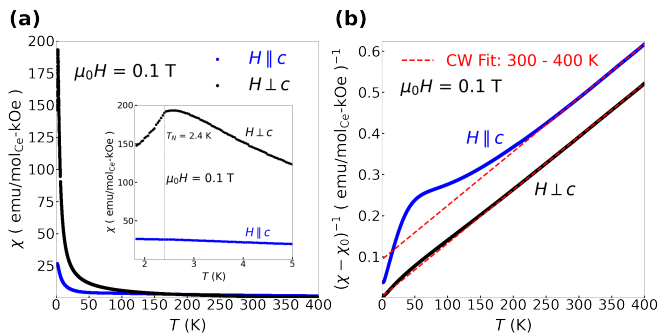


FIG. 2. (a) Magnetic susceptibility of crystal *A* taken in 0.1 T of applied magnetic field with the field aligned perpendicular to the *c*-axis (black) and parallel to the *c*-axis (blue). The inset shows the low temperature magnetic susceptibility with the magnetic transition at $T_N = 2.4$ K marked by the vertical dashed line. (b) Inverse magnetic susceptibility from the same measurement with a Curie-Weiss fit between 300–400 K (dashed, red curve).

Figure 2(b) shows the inverse magnetic susceptibility (with the T -independent offset χ_0 subtracted from the susceptibility) for both orientations of the crystal. The data was fit between 300–400 K (dashed, red curve) by a Curie-Weiss model with a constant offset via the following equation:

$$\chi = \frac{1}{T - \theta_{CW}} \frac{N_A}{3k_B} \mu_{eff}^2 + \chi_0 \quad (13)$$

where χ is the magnetic susceptibility per mole, θ_{CW} is the Curie temperature, N_A Avogadro's number, χ_0 is the T -independent susceptibility component, and μ_{eff} is the effective moment in units of μ_B . The parameters obtained from this fit are displayed in Table I. The effective moments for both orientations show good agreement with the free-space effective Ce^{3+} moment of $2.54 \mu_B$. The high temperature Curie-Weiss fit of the data deviates strongly under 200 K due to the strong effects of the crystal field in this orientation.

TABLE I. Parameters from the Curie-Weiss fit of Ce_2SnS_5 crystal *A* between 300 K - 400 K in a field of $\mu_0 H = 0.1$ T aligned both perpendicular and parallel to the *c*-axis.

Parameter	$H \perp c$	$H \parallel c$
θ_{CW} (K)	-2.13	-70.9
μ_{eff} (μ_B/Ce)	2.48	2.47

Figure 3 shows the magnetization as a function of applied magnetic field both perpendicular and parallel to the *c*-axis. When the field is applied perpendicular to the *c*-axis (at $T = 1.8$ K, below T_N) the magnetization reaches $1.15 \mu_B$ per cerium atom at $\mu_0 H = 7$ T and appears to saturate. At $T = 1.8$ K, the magnetization also

exhibits an inflection point near $\mu_0 H = 1$ T; this inflection point disappears for temperatures above T_N whereat the magnetization follows a standard Brillouin function. When the field is applied parallel to the *c*-axis, the magnetic susceptibility remains linear up to $\mu_0 H = 7$ T for all temperatures.

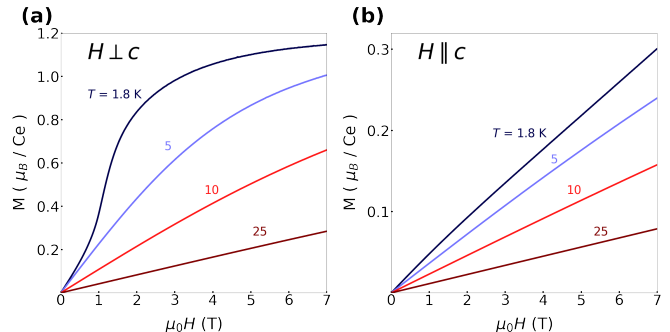


FIG. 3. Magnetization of crystal *A* taken as a function of applied magnetic field perpendicular to the *c*-axis (a) and parallel to the *c*-axis (b). The magnetization was measured at several temperatures both below and above $T_N = 2.4$ K and is presented in units of μ_B per cerium atom.

The low temperature magnetization was fit to the expected magnetization of a single Kramers' doublet (see Appendix A) to yield ground state g -factors of $g_{\parallel} = 1.2$ and $g_{\perp} = 2.5$ which are very close to the values predicted for the ground state spanned by $|\psi_{\pm 1/2}\rangle$. The experimentally determined ground state value of g_{\parallel} is larger than the expected value of $6/7$ for this doublet due to thermal population of the excited Kramers' doublets mixing in larger, nonzero values of g_{\parallel} . The expected saturation magnetizations of the $|\psi_{\pm 1/2}\rangle$ doublet are $M_s^{\parallel} = \frac{1}{2}g_{\parallel} = 3/7$ and $M_s^{\perp} = \frac{1}{2}g_{\perp} = 9/7$; these values are consistent with the behavior of the magnetization seen in Fig. 3.

B. Heat Capacity

Heat capacity was measured using a Quantum Design PPMS system with the heat capacity module enabled. Single crystals were affixed to heater platform using Apiezon N grease. A background heat capacity measurement was taken of the grease prior to mounting the crystal such that it could be subtracted from the total heat capacity after the crystal was mounted.

Figure 4 shows the heat capacity of Ce_2SnS_5 in zero field. This data was fit above 25 K with a combined Debye and Einstein phonon model (see Appendix B for more details) such that the extrapolated fit could serve as a phonon background under 25 K. The inset of Fig. 4 shows the magnetic heat capacity C_M obtained by subtracting this phonon background from the data in this temperature regime. The data below the $T_N = 2.4$ K transition was fit by a $C_M \sim T^{\alpha}$ power law to obtain

the exponent $\alpha = 3.03$ which is consistent with the heat capacity of antiferromagnetic magnons in three dimensions.

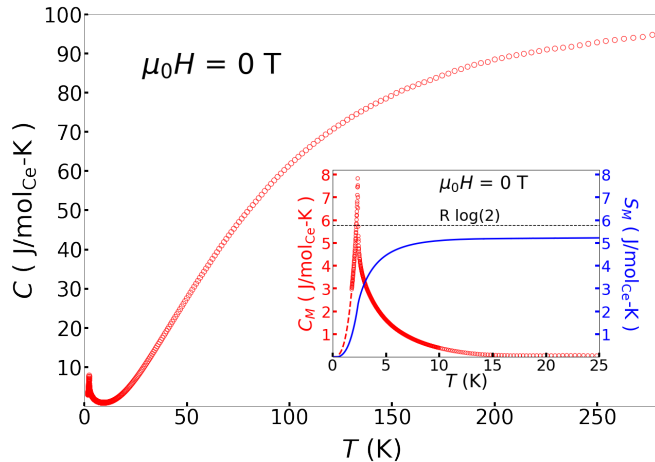


FIG. 4. Heat capacity of crystal *B* taken in zero field showing the magnetic transition at $T_N = 2.4$ K. The inset shows the magnetic part of the heat capacity and the computed magnetic entropy below 25 K. The magnetic entropy lost through the transition is consistent with the doublet ground state of the cerium *4f*-electron level structure.

This power law fit was used to extrapolate the data down to zero temperature and provide a continuous magnetic heat capacity function for computing the magnetic entropy S_M . The magnetic entropy saturates to a value of $R \log \Omega$ with $\Omega = 1.87$ which agrees with the predicted doublet ground state of the Ce^{3+} level structure.

Figure 5 shows the evolution of the magnetic transition in increasing magnetic fields applied both perpendicular and parallel to the *c*-axis. For field applied perpendicular to the *c*-axis, the peak persists above 1.8 K until at least $\mu_0 H = 0.9$ T. For field applied parallel to the *c*-axis persists above 1.8 K until at least $\mu_0 H = 5$ T.

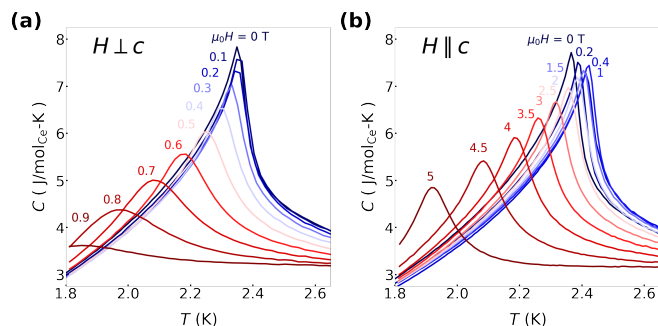


FIG. 5. Heat capacity measured around the magnetic transition for various applied magnetic fields. (a) Heat capacity of crystal *B* with field aligned perpendicular to the *c*-axis. (b) Heat capacity of crystal *C* with field aligned parallel to the *c*-axis.

For both orientations of the crystal relative to the ap-

plied magnetic field, heat capacity measurements were taken up to 9 T to reveal a large Schottky anomaly. This Schottky anomaly arises from the Ce^{3+} electronic level structure, as ^{140}Ce (the primary isotope in natural cerium) does not possess a nuclear moment and thereby does not exhibit a nuclear Schottky anomaly. The behavior of the Schottky anomaly for both orientations of the crystal is discussed further in Appendix C.

C. Phase Diagram

The anisotropy in the magnetic ordering of Ce_2SnS_5 is illustrated in the phase diagram shown in Figure 6 derived from heat capacity and magnetization data with field applied both perpendicular and parallel to the *c*-axis. The phase boundaries could only be experimentally measured down to 1.8 K, but an upper bound on the critical field corresponding to $T = 0$ can be determined by the field at which the Schottky anomaly emerges above 1.8 K.

Figure 6(a) shows the phase boundary when field is applied perpendicular to the *c*-axis. It derives the transition temperature T_N from the position of the peak in heat capacity (red triangle marker) and magnetization (blue circle marker) measured in fixed field. It also plots the critical field H_C (green square marker) corresponding to the kink in magnetization measured at fixed temperature. The value of H_C was determined from the position of the extremum of the second derivative of magnetization with respect to field.

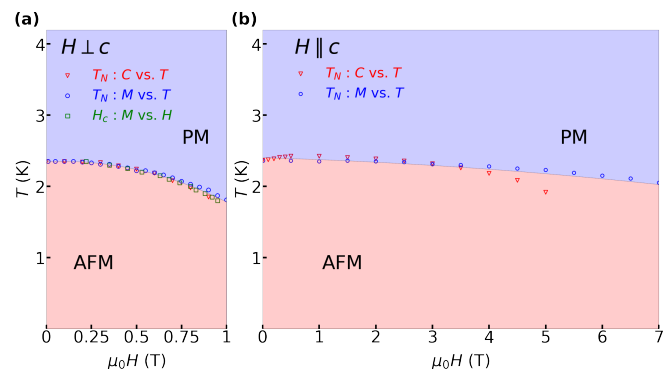


FIG. 6. Phase diagram for Ce_2SnS_5 with field applied perpendicular (a) and parallel (b) to the *c*-axis showing the boundary between antiferromagnetism (AFM) and paramagnetism (PM). The data is derived from the position T_N of the features in heat capacity (red triangle) and magnetization (blue circle) measured in fixed field, and the position of the kink at H_C in magnetization (green square) measured at fixed temperature.

Figure 6(b) describes the phase boundary when field is applied parallel to the *c*-axis. It contains values of T_N derived from the the position of the peak heat capacity (red triangle marker) as well as the kink in the magnetization

(blue circle marker) measured in fixed field. The location of the kink in magnetization was determined from the position of the extremum of the first derivative of magnetization with respect to temperature.

D. Powder Neutron Scattering

Powder neutron diffraction was performed at Oak Ridge National Laboratory using the HB-2A diffractometer at the High Flux Isotope Reactor (HFIR). Four grams of powdered Ce_2SnS_5 were sealed under helium in an aluminum sample can and a ^3He cryostat was used to cool the sample under 2 K. Neutron scattering spectra ($\lambda = 2.41 \text{ \AA}$) were taken in zero field at several temperatures between 300 mK and 4 K.

Figure 7(a) shows the diffraction peaks associated with magnetic reflections that appear below $T_N = 2.4 \text{ K}$; a 4 K spectrum provided a high temperature background to subtract from spectra taken under 2.4 K. Each background subtracted magnetic reflection peak (ten in total) was fit with a Lorentzian lineshape to extract the peak center q_0 (see Appendix D for more details on this fit). These values of q_0 were used to determine the best fitting commensurate propagation vectors associated with the magnetic unit cell using the k-search program in the FullProf Suite.

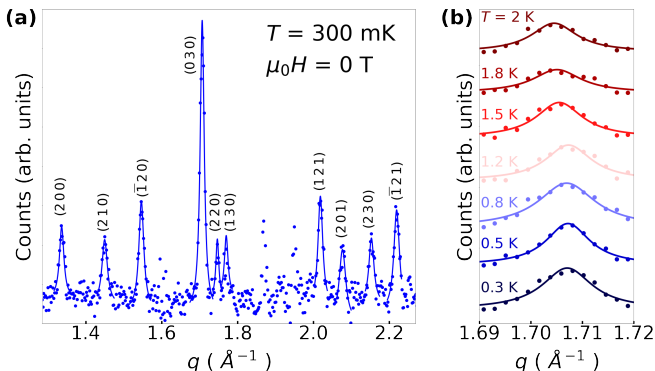


FIG. 7. (a) Zero-field, background-subtracted powder neutron diffraction spectrum ($\lambda = 2.41 \text{ \AA}$) of Ce_2SnS_5 at 300 mK. The Lorentzian fits (as well as the (hkl) indices) of each magnetic reflection peak are shown. Note that the (421) magnetic peak occurs near $q_0 = 3.5 \text{ \AA}^{-1}$ and is not shown here. (b) Temperature evolution of the fourth magnetic reflection peak ((030) at 300 mK) showing the shifting behavior under T_N before locking into a fixed position under 1.2 K.

Below approximately 1.2 K, the best commensurate propagation vector was $(q_x, q_y, q_z) = (1/3, 0, 0)$; the system appears to lock into this at low temperatures. The shifting of the magnetic reflection peaks as the system is cooled down to 1.2 K suggests the presence of incommensurate order just below T_N which eventually locks into commensurate order. Figure 7(b) shows this shifting behavior for the fourth magnetic reflection peak ((030)

at 300 mK). Appendix D presents a table showing all the magnetic peak locations q_0 for each temperature a spectrum was measured.

V. DISCUSSION

The Ce_2SnS_5 system realizes highly anisotropic magnetic order at low temperatures in a reduced symmetry environment provided by the distorted TTP crystal field surrounding each cerium site. From measurements of the perpendicular and parallel components of the g -tensor, the ground state is described by the Γ_7 Kramers' doublet in the TTP crystal electric field. In this environment, the magnetic order appears to be more resilient to magnetic fields applied parallel to the c -axis compared to fields applied perpendicular to the c -axis. We hypothesize that this behavior arises from XY-like anisotropy which biases the magnetic moments to point in the ab -plane.

Such a magnetic ordering is supported by the magnetization response illustrated in Figure 3. Due to the strong in-plane anisotropy, when the applied magnetic field is oriented perpendicular to the c -axis, the moments point in the same plane as the field such that it drives the system out of the ordered phase above approximately 1 T and allows the magnetization to saturate by 7 T. When the field is oriented near parallel to the c -axis, the moments point almost orthogonally to it such that increasing the field only serves to cant the moments out of the ab -plane; this effect is weak enough not to saturate the magnetization even by 7 T at 1.8 K in this orientation. Above the ordering temperature, the ratio g_\perp/g_\parallel was found to be approximately two (see Appendix A). This anisotropy in the moment induced by the crystal field suggests XY-like behavior for temperatures $T > T_N$ in the paramagnetic phase.

Magnetic susceptibility measured for $T < T_N$ suggests that the system realizes antiferromagnetic order as the magnetization decreases as temperature decreases below T_N (inset of Fig. 2(a)). Powder neutron diffraction reveals magnetic reflection peaks that shift as the temperature decreases below T_N until they eventually lock into a magnetic phase with the commensurate magnetic propagation vector of $(q_x, q_y, q_z) = (1/3, 0, 0)$ below approximately 1.2 K. This behavior suggests the presence of incommensurate order just below T_N before the system locks into a commensurate magnetic structure upon cooling. Additional neutron diffraction measurements on single crystals would be an important future research direction to determine the true magnetic structure.

VI. CONCLUSION

The presented data shows that the Ce_2SnS_5 system exhibits strong in-plane magnetic anisotropy arising from the TTP crystal field surrounding the cerium site. In the paramagnetic phase, the system is characterized by an

anisotropic g-tensor closely matching the expected magnetic behavior of the ground state Γ_7 Kramers' doublet. The system realizes magnetic order upon cooling below $T_N = 2.4\text{K}$ and the magnetic entropy associated with the zero-field peak in heat capacity affirms the doublet nature of the ground state. Powder neutron diffraction shows that the zero-field ordered phase exhibits incommensurate order that shifts the positions of the magnetic reflections as the system cools below T_N .

The strong magnetic anisotropy in the system suggests that it realizes three dimensional XY model physics. Ce_2SnS_5 provides a simple material platform to study the interplay between incommensurate order and the XY model. Future single crystal neutron diffraction measurements in nonzero field will be needed to determine the potentially complicated magnetic phase diagram. Critical exponents computed from order parameter measurements obtained from neutron diffraction would also serve to tie the system to the XY model.

ACKNOWLEDGMENTS

We acknowledge D. Yahne and S. Calder for support with the neutron scattering experiment. This work was funded, in part, by the Gordon and Betty Moore Foundation EPiQS Initiative, Grant No. GBMF9070 to J.G.C (instrumentation development) and the Army Research Office, Grant No. W911NF-24-1-0234 (material characterization). A portion of this research used resources at the High Flux Isotope Reactor, a DOE Office of Science User Facility operated by the Oak Ridge National Laboratory. The beam time was allocated to HB-2A on proposal number 32050.1.

Appendix A: Magnetization of the Kramers' Doublets

The D_{3h} local crystal field breaks up the originally sixfold degenerate manifold of $J = 5/2$ states into three Kramers' doublets. The Hamiltonian describing the Zeeman splitting is given by:

$$\mathbf{H} = \mu_B \vec{H} \cdot \overset{\leftrightarrow}{g} \cdot \vec{\mathbf{J}} \quad (\text{A1})$$

where $\vec{\mathbf{J}}$ is the angular momentum operator (in units of \hbar), $\overset{\leftrightarrow}{g}$ is the g-tensor, and \vec{H} is the magnetic field [12, 13]. In free-space, Eq. (A1) reduces to:

$$\mathbf{H} = \mu_B g_J (H_x \mathbf{J}^x + H_y \mathbf{J}^y + H_z \mathbf{J}^z) \quad (\text{A2})$$

since the g-tensor is proportional to the identity operator. The Hamiltonian in Eq. (A2) may be projected onto the $|J = 5/2, \pm m_J\rangle$ Kramers' doublets of the D_{3h} crystal field to yield:

$$\mathbf{H}_{\pm 1/2} = \frac{3}{7} \begin{pmatrix} H_z & 3(H_x - iH_y) \\ 3(H_x + iH_y) & -H_z \end{pmatrix} \mu_B \quad (\text{A3})$$

$$\mathbf{H}_{\pm 3/2} = \frac{9}{7} \begin{pmatrix} H_z & 0 \\ 0 & -H_z \end{pmatrix} \mu_B \quad (\text{A4})$$

$$\mathbf{H}_{\pm 5/2} = \frac{15}{7} \begin{pmatrix} H_z & 0 \\ 0 & -H_z \end{pmatrix} \mu_B \quad (\text{A5})$$

where the Landé g-factor of $g_{J=5/2} = 6/7$ was used [12]. These projected hamiltonians may be rewritten in the form of Eq. (A1) as follows:

$$\mathbf{H}_{\pm 1/2} = \mu_B \begin{pmatrix} H_x \\ H_y \\ H_z \end{pmatrix}^\top \begin{pmatrix} \frac{18}{7} & 0 & 0 \\ 0 & \frac{18}{7} & 0 \\ 0 & 0 & \frac{6}{7} \end{pmatrix} \begin{pmatrix} \tilde{\mathbf{S}}^x \\ \tilde{\mathbf{S}}^y \\ \tilde{\mathbf{S}}^z \end{pmatrix} \quad (\text{A6})$$

$$\mathbf{H}_{\pm 3/2} = \mu_B \begin{pmatrix} H_x \\ H_y \\ H_z \end{pmatrix}^\top \begin{pmatrix} 0 & 0 & 0 \\ 0 & 0 & 0 \\ 0 & 0 & \frac{18}{7} \end{pmatrix} \begin{pmatrix} \tilde{\mathbf{S}}^x \\ \tilde{\mathbf{S}}^y \\ \tilde{\mathbf{S}}^z \end{pmatrix} \quad (\text{A7})$$

$$\mathbf{H}_{\pm 5/2} = \mu_B \begin{pmatrix} H_x \\ H_y \\ H_z \end{pmatrix}^\top \begin{pmatrix} 0 & 0 & 0 \\ 0 & 0 & 0 \\ 0 & 0 & \frac{30}{7} \end{pmatrix} \begin{pmatrix} \tilde{\mathbf{S}}^x \\ \tilde{\mathbf{S}}^y \\ \tilde{\mathbf{S}}^z \end{pmatrix} \quad (\text{A8})$$

where $\tilde{\mathbf{S}}^\alpha$ are the "effective" spin-1/2 angular momentum operators written in terms of the 2×2 Pauli operators as $\tilde{\mathbf{S}}^\alpha = \frac{1}{2} \boldsymbol{\sigma}^\alpha$ [13]. The components g_{\parallel} (parallel to \hat{z} -axis) and g_{\perp} (perpendicular to \hat{z} -axis) may then be read off of the g-tensor in these hamiltonians for each Kramers' doublet.

The Zeeman hamiltonian has been projected onto these Kramers' doublets such that each doublet effectively functions as a spin-1/2 system with eigenenergies of $E_{\pm} = \pm \frac{1}{2} g_{\parallel, \perp} \mu_B H$ depending on the direction of the applied magnetic field to the \hat{z} -axis set by the principle rotation axis of the crystal field. The expected magnetization of each Kramers' doublet then follows the standard spin-1/2 form with $\mu \equiv \frac{1}{2} g_{\parallel, \perp} \mu_B$ shown in Eq. (A9).

$$M = \frac{1}{2} g_{\parallel, \perp} \mu_B \tanh \left(\frac{g_{\parallel, \perp} \mu_B H}{2k_B T} \right) \quad (\text{A9})$$

The low temperature magnetization may be fit by Eq. (A9) both as a function of temperature, and as a function of field to extract $g_{\parallel, \perp}$ for the ground state Kramers' doublet under the assumption that this is the only populated energy level at such low temperatures.

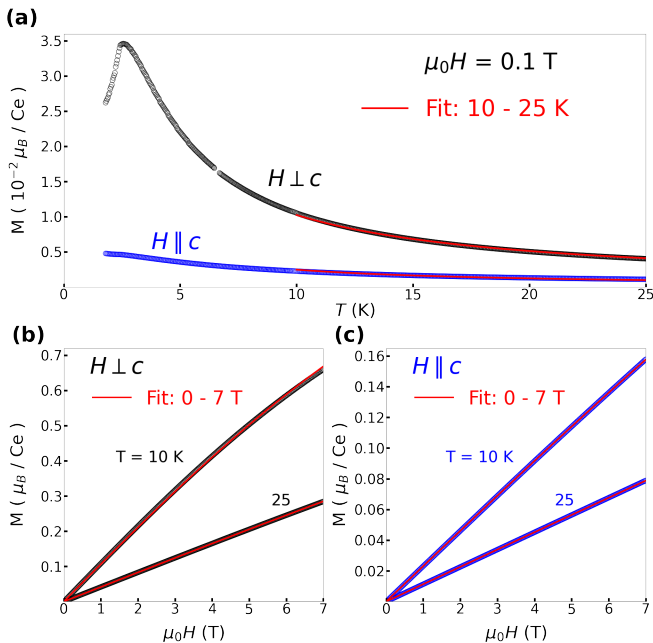


FIG. 8. Magnetization of crystal *A* measured as a function of (a) temperature at fixed field (0.1 T), and as a function of (b, c) field at fixed temperature (10 and 25 K). Measurements were taken with field aligned perpendicular to the *c*-axis (black) and parallel to the *c*-axis (blue). The dashed red line shows the fit of the magnetization using Eq. (A9).

Figure 8 shows this fit for both orientations of the crystal relative to the magnetic field. Note that due to the orientation of the CEF potential in Eq. (5) relative to the crystal structure, g_{\parallel} is extracted from the measurement when field is parallel to the *c*-axis, and g_{\perp} is extracted from the measurement when field is perpendicular to the *c*-axis. The g-factors for the ground state extracted by this fit are presented in Table II along with the values predicted for the ground state spanned by $|\psi_{\pm 1/2}\rangle$.

TABLE II. Ground state g-factors extracted for Ce_2SnS_5 crystal *A* by fitting magnetization vs. temperature at 0.1 T from 5 – 10 K and magnetization vs. field at 5 and 10 K from 0 – 7 T.

	g_{\perp}	g_{\parallel}	g_{\perp}/g_{\parallel}
Predicted for $ \psi_{\pm 1/2}\rangle$	18/7	6/7	3
M vs. H at 10 K	2.517	1.172	2.147
M vs. H at 25 K	2.484	1.297	1.915
M vs. T at 0.1 T	2.470	1.213	2.035

Appendix B: Fitting the Heat Capacity

The heat capacity of Ce_2SnS_5 is modeled extremely well by phonon mode contributions in the region well above the magnetic transition. This phonon contribution

serves as a background at low temperatures such that the magnetic contributions to heat capacity may be isolated and the magnetic heat capacity computed. The phonon heat capacity of the system may be fit via a combined anharmonic Einstein and Debye model as given by [14]:

$$\frac{C}{Nk_B} = \sum_{j \in \text{optic}} \frac{1}{1 - C_j T} \frac{\epsilon_j^2 e^{\epsilon_j/T}}{(e^{\epsilon_j/T} - 1)^2} + \frac{9}{1 - C_D T} \left(\frac{T}{\theta_D}\right)^3 \int_0^{\theta_D/T} \frac{x^4 e^x dx}{(e^x - 1)^2} \quad (\text{B1})$$

where θ_D is the Debye temperature. The summation in the Einstein term is over all optic modes and $\epsilon_j = \hbar\omega_j/k_B$ is the energy (in units of temperature) of the optic mode with frequency ω_j . The anharmonicities of the optic modes and the Debye term are given by C_j and C_D respectively; in this model, the oscillator frequency ω_j is given by [14]:

$$\omega_j = \omega_0 (1 - C_j T) \quad (\text{B2})$$

where ω_0 is the harmonic oscillator frequency and C_j is the anharmonicity. Based on Eq. (B1), the phonon term of the heat capacity may be fit using the following model:

$$C_{ph} \sim 3\alpha(1 + C_E T) \frac{\epsilon^2 e^{\epsilon/T}}{(e^{\epsilon/T} - 1)^2} + 9(1 - \alpha)(1 + C_D T) \left(\frac{T}{\theta_D}\right)^3 \int_0^{\theta_D/T} \frac{x^4 e^x dx}{(e^x - 1)^2} \quad (\text{B3})$$

where $0 \leq \alpha \leq 1$ is an interpolation parameter between the Einstein and Debye terms. In Eq. (B3), it is assumed that there is only one branch of isotropic optic modes in three dimensions, and that the anharmonicities are small such that $(1 - C_j T)^{-1} \approx (1 + C_j T)$. The inclusion of the anharmonicities allows the model to remain valid up to higher temperatures whereat the anharmonic effects become evident.

The heat capacity data was fit between 25 K and 300 K (well above $T_N = 2.4$ K) to yield a Debye temperature of $\theta_D = 198$ K, and an optic mode energy of $\epsilon = 348$ K. The interpolation parameter was $\alpha = 0.51$ and the anharmonicities of the Debye and Einstein terms were $C_D = 2.2 \times 10^{-4} \text{ K}^{-1}$ and $C_E = 3.4 \times 10^{-19} \text{ K}^{-1}$ respectively. This fit along with the heat capacity data is shown in Fig. 9. Note that the apparent feature in the data near 300 K is a measurement anomaly likely due to freezing of grease in the cryostat upon cooling.

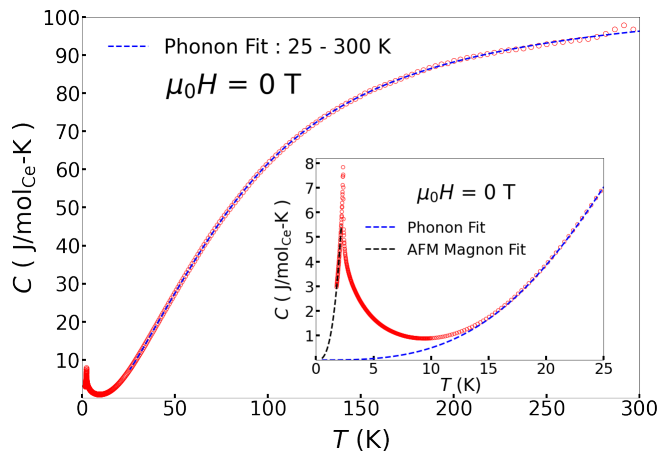


FIG. 9. Zero-field heat capacity of Ce_2SnS_5 with the phonon fit (between 25 K and 300 K) drawn in blue. The inset shows the phonon fit extrapolated below 25 K (dashed blue line) as well as the AFM magnon fit (dashed black line) extrapolated below 1.8 K.

The model in Eq. (B3) is applied in the high-temperature, phonon-dominated region of the measurement such that it may provide an appropriate extrapolated background for analysis of the low temperature regime where magnetic interactions become relevant. The inset of Fig. 9 shows the extrapolated high temperature phonon fit in blue; this fit remains smooth and does not cross the data such that it provides a high quality background.

The dashed black line in the inset of Fig. 9 is the antiferromagnetic (AFM) magnon fit below the Neel temperature. This was fit via a $C_M \sim T^\alpha$ power law between 1.8 K and 2.2 K to yield an exponent of $\alpha = 3.03$ which agrees well with the prediction for three-dimensional AF magnons. In three dimensions, magnons are expected to exhibit a $C \sim T^{3/2}$ heat capacity in a ferromagnetically ordered system. Since an antiferromagnetic lattice can be broken up into a bipartite sum of ferromagnetic sublattices, an AF lattice with two such sublattices exhibit a $C \sim T^3$ heat capacity. This simple functional form was used to extrapolate the heat capacity from 1.8 K to zero to allow for the magnetic entropy to be computed.

Appendix C: The Schottky Anomaly

The Ce_2SnS_5 system exhibits a pronounced Schottky anomaly in magnetic fields strong enough to extinguish the magnetic order. For fields perpendicular to the c -axis, this occurs roughly above $\mu_0 H = 1$ T. For fields parallel to the c -axis, this occurs roughly above $\mu_0 H = 5.5$ T. Fig. 10 shows the evolution of the Schottky anomaly in field for both crystal orientations.

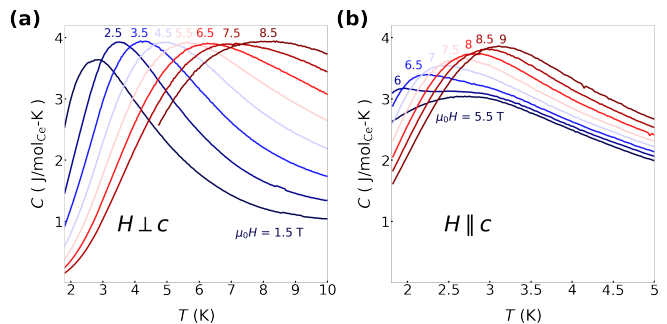


FIG. 10. Evolution of the Schottky anomaly in various applied magnetic fields. (a) Heat capacity of crystal B with field aligned perpendicular to the c -axis. (b) Heat capacity of crystal C with field aligned parallel to the c -axis.

The Schottky anomaly was unable to be fit at such high fields due to the number of relevant free parameters. Due to the crystal field distortion, the relevant g -factors differ from those computed in Eqs. (10 - 12) and the exact values become important at high fields which necessitates their being fit as free parameters. Due to the lack of a zero-field Schottky anomaly, the two zero-field energy level splittings also need to be fit at high field. The resulting five-parameter did not converge to consistent values for measurements at different fields for the same crystal orientation.

Appendix D: Fitting the Magnetic Reflection Peaks

The powder neutron diffraction spectra taken under $T_N = 2.4$ K show several magnetic reflections which appear at q -vectors distinct from the nuclear reflections. To fit these distinct magnetic reflection peaks, a 4 K background spectrum was subtracted from the spectra taken under T_N , and each peak was fit with a Lorentzian lineshape:

$$f(q) = A \frac{\gamma^2}{\gamma^2 + (q - q_0)^2} + f_0 \quad (\text{D1})$$

where A is the peak amplitude, γ is the linewidth scale, q_0 is the peak location, and f_0 is a constant offset.

The variance of each data point in the background subtracted spectrum was obtained by adding the variances of the background spectrum to that of the spectrum taken under T_N . A least-squares fit of the Lorentzian lineshape described in Eq. (D1) was then performed on the background subtracted dataset around each magnetic reflection peak to extract its position q_0 . The standard deviation of the q_0 extracted from the fit was obtained by taking the square root of the corresponding diagonal element of the covariance matrix of the fit. Tables III and IV shows the q_0 values extracted by this fit as well as the corresponding standard deviation σ_{q_0} for each of these magnetic reflection peaks.

TABLE III. Peak locations (q_0) and standard deviations (σ_{q_0}) extracted from Lorentzian fits of the magnetic reflection peaks of Ce_2SnS_5 obtained from zero-field powder neutron diffraction at several temperatures under $T_N = 2.4$ K. The peak numbers correspond with the following (hkl) indices at 300 mK: **1** - (200), **2** - (210), **3** - ($\bar{1}20$), **4** - (030), **6** - (121), **7** - (210), **8** - ($\bar{1}21$), **9** - (200), and **10** - (421).

Peak	T (K)	q_0 (\AA^{-1})	σ_{q_0} (10^{-3}\AA^{-1})	Peak	T (K)	q_0 (\AA^{-1})	σ_{q_0} (10^{-3}\AA^{-1})	Peak	T (K)	q_0 (\AA^{-1})	σ_{q_0} (10^{-3}\AA^{-1})
1	2.0	1.3525	1.1835	4	2.0	1.7046	0.4102	8	2.0	2.1619	1.2449
	1.8	1.3494	0.8948		1.8	1.7050	0.4814		1.8	2.1618	1.4510
	1.5	1.3453	0.7693		1.5	1.7054	0.3473		1.5	2.1591	0.9034
	1.2	1.3366	1.0482		1.2	1.7071	0.3306		1.2	2.1539	1.0455
	0.8	1.3351	1.0573		0.8	1.7068	0.3038		0.8	2.1539	1.2701
	0.5	1.3363	0.7847		0.5	1.7070	0.2899		0.5	2.1545	0.9207
	0.3	1.3365	0.5752		0.3	1.7069	0.1773		0.3	2.1529	0.6095
2	2.0	1.4628	1.2474	6	2.0	2.0226	0.7943	9	2.0	2.2142	1.0023
	1.8	1.4622	1.4791		1.8	2.0220	0.6803		1.8	2.2148	0.7947
	1.5	1.4581	1.4895		1.5	2.0203	0.6518		1.5	2.2149	0.7677
	1.2	1.4519	0.6417		1.2	2.0178	0.5832		1.2	2.2196	0.7110
	0.8	1.4503	0.8340		0.8	2.0183	0.4941		0.8	2.2178	0.7361
	0.5	1.4518	0.7701		0.5	2.0181	0.6343		0.5	2.2197	0.6646
	0.3	1.4498	0.6504		0.3	2.0184	0.3656		0.3	2.2194	0.4627
3	2.0	1.5361	0.7864	7	2.0	2.0885	1.2205	10	2.0	3.5273	1.6729
	1.8	1.5376	0.8419		1.8	2.0871	2.0735		1.8	3.5295	1.7698
	1.5	1.5397	0.5757		1.5	2.0824	0.8781		1.5	3.5291	0.7773
	1.2	1.5467	0.5495		1.2	2.0765	1.0520		1.2	3.5300	0.8236
	0.8	1.5461	0.7012		0.8	2.0769	1.0830		0.8	3.5302	0.7955
	0.5	1.5475	0.6549		0.5	2.0767	1.1134		0.5	3.5295	1.2196
	0.3	1.5465	0.3876		0.3	2.0766	0.6701		0.3	3.5295	0.5814

TABLE IV. Peak locations (q_0) and standard deviations (σ_{q_0}) extracted from Lorentzian fits of the split peak $\mathbf{5}_L/\mathbf{5}_R$. Note that this magnetic reflection peak bifurcates under 1.5 K (see Fig. 7(a)); the corresponding (hkl) indices at 300 mK are: $\mathbf{5}_L$ - (220) and $\mathbf{5}_R$ - (130).

T (K)	q_0 (\AA^{-1})		σ_{q_0} (10^{-3}\AA^{-1})	
2.0	1.7576		1.6542	
1.8	1.7652		1.4265	
1.5	1.7662		2.9768	
1.2	1.7473	1.7687	1.1387	1.0384
0.8	1.7455	1.7673	1.1534	0.9714
0.5	1.7481	1.7709	1.3322	1.3299
0.3	1.7468	1.7702	0.6484	1.0341

-
- [1] A. Wildes, V. Simonet, E. Ressouche, R. Ballou, and G. McIntyre, The magnetic properties and structure of the quasi-two-dimensional antiferromagnet CoPS_3 , *Journal of Physics: Condensed Matter* **29**, 455801 (2017).
- [2] P. A. Joy and S. Vasudevan, Magnetism in the layered transition-metal thiophosphates MPS_3 (M=Mn, Fe, and Ni), *Phys. Rev. B* **46**, 5425 (1992).
- [3] V. Grasso and L. Silipigni, Low-dimensional materials: The MPX_3 family, physical features and potential future applications, *La Rivista del Nuovo Cimento* **25**, 1 (2002).
- [4] L. Regnault, J. Rossat-Mignod, J. Henry, R. Pynn, and D. Petitgrand, Magnetic excitations in the quasi-2d planar magnets $\text{BaM}_2(\text{XO}_4)_2$ (M= Co, Ni; X= P, As, in *Magnetic Excitations and Fluctuations: Proceedings of an International Workshop, San Miniato, Italy, May 28–June 1, 1984* (Springer, 1984) pp. 201–206.
- [5] L. J. d. Jongh, *Magnetic properties of layered transition metal compounds*, Physics and chemistry of materials with low-dimensional structures, Vol. 9 (Kluwer Academic Publishers, Dordrecht, 1990).
- [6] P. S. Jaulmes, Structure cristalline du sulfure d'étain et de lanthane, La_2SnS_5 , *Acta Crystallographica Section B: Structural Crystallography and Crystal Chemistry* **30**, 2283 (1974).
- [7] M. Guittard, M. Julien-Pouzol, and S. Jaulmes, Systems $\text{Ln}_2\text{X}_3\text{-SnX}_2$ (Ln = terres rares et X = S ou Se) composés Ln_2SnS_5 , définition et étude structurale, *Materials Research Bulletin* **11**, 1073 (1976).
- [8] K. Momma and F. Izumi, Vesta 3 for three-dimensional visualization of crystal, volumetric and morphology data, *J. Appl. Crystallogr.* **44**, 1272 (2011).
- [9] J. Jensen and A. R. Mackintosh, Elements Of Rare Earth Magnetism, in *Rare Earth Magnetism: Structures and Excitations* (Oxford University Press, 1991) <https://academic.oup.com/book/0/chapter/422683517/chapter-pdf/52583750/isbn-9780198520276-book-part-1.pdf>.
- [10] M. Tinkham, *Group Theory and Quantum Mechanics* (Dover Publications, 2003).
- [11] K. A. Gschneidner and L. Eyring, eds., *Handbook on the Physics and Chemistry of Rare Earths*, Vol. 23 (Elsevier, 1996).
- [12] N. M. Atherton, *Electron Spin Resonance: Theory and Applications* (E. Horwood; Halsted Press, Chichester [England], New York, 1973).
- [13] A. Abragam and B. B. Bleaney, *Electron paramagnetic resonance of transition ions*, International series of monographs on physics (Clarendon P., Oxford, 1970).
- [14] C. A. Martin, Simple treatment of anharmonic effects on the specific heat, *Journal of Physics: Condensed Matter* **3**, 5967 (1991).